Electronic Supplementary Material (ESI) for Environmental Science: Nano.

Electronic Supplementary Information

Nickel enrichment of next-generation NMC nanomaterials alters material stability, causing unexpected dissolution behavior and observed toxicity to *S. oneidensis* MR-1 and *D. magna*

Joseph T. Buchman[§], Evan A. Bennett[†], Chenyu Wang[‡], Ali Abbaspour Tamijani[‖], Joseph W. Bennett[‖], Blake G. Hudson[‖], Curtis M. Green[‡], Peter L. Clement[§], Bo Zhi[§], Austin H. Henke[‡], Elizabeth D. Laudadio[‡], Sara E. Mason[‖], Robert J. Hamers[‡], Rebecca D. Klaper[†], Christy L. Haynes[§]

[§]Department of Chemistry, University of Minnesota, Minneapolis, MN 55455, United States

[†]School of Freshwater Sciences, University of Wisconsin-Milwaukee, Milwaukee, WI 53204

[‡]Department of Chemistry, University of Wisconsin, Madison, WI 53706, United States

[‖]Department of Chemistry, University of Iowa, Iowa City, Iowa 52242, United States

S1. Materials

Commercial 333, 622, and 811 NMC (referred to as c333, c622, and c811 NMC) were acquired from Electrodes and More (Richardson, TX).

S2. Surface Area Determination of Commercial NMC

As described in the manuscript for surface area determination of nanoscale NMC, the commercial NMC was measured using a Micromeritics Gemini VII 2390 surface area analyzer. The sample holder was loaded with ~100 mg of commercial 622 and commercial 811 NMC samples. The degas conditions were the same as for nanoscale NMC, and the relative pressure range (P/P_0) of 0.05-0.3 was used for analysis of surface area. Being microscale materials, the commercial NMC samples had much lower surface areas than the nanoscale materials presented in the main text, with c622 NMC being 0.536 m^2/g and c811 NMC at 0.956 m^2/g. These surface areas were used to inform the surface area-based dosing of cNMC to *S. oneidensis*.

S3. Energy-dispersive X-ray Spectroscopy gives Stoichiometry of c622 and c811 NMC

EDS spectra were acquired using an Oxford INCAx-sight EDS which was paired with a T12 transmission electron microscope. The reported atomic percentages were used to determine the transition metal ratios in the materials. The stoichiometries as reported by EDS for c622 and c811 NMC were $Li_xNi_{0.57}Mn_{0.19}Co_{0.23}O_2$ and $Li_xNi_{0.78}Mn_{0.12}Co_{0.10}O_2$, respectively, correlating well with the expected stoichiometry. Note that lithium cannot be quantified by EDS due to limitations of the technique.[1]

S4. Powder X-ray Diffraction

To analyze the structure of NMC materials, a Bruker D8 Advance Powder X-ray diffractometer with a Cu Kα source was used. The NMC powder was deposited onto SiO_2 zero diffraction plate (MTI Corporation, Richmond, CA) and smoothed out with a spatula before analysis. The XRD patterns reveal similar crystal structure between 333 and 622 NMC.

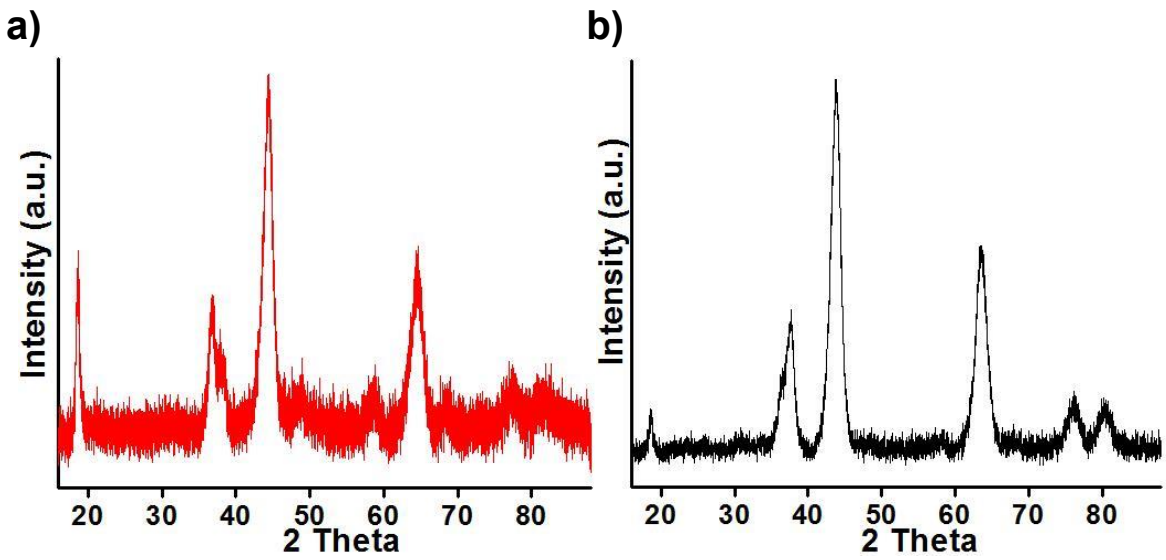

Figure S1. XRD patterns for a) 333 NMC and b) 622 NMC.

S5. Transmission Electron Microscopy

From TEM images of the different materials, it can be seen that 333 and 622 NMC are nanoscale particles that display a sheet-like morphology. On the other hand, commercially-obtained c622 and c811 NMC are microscale materials.

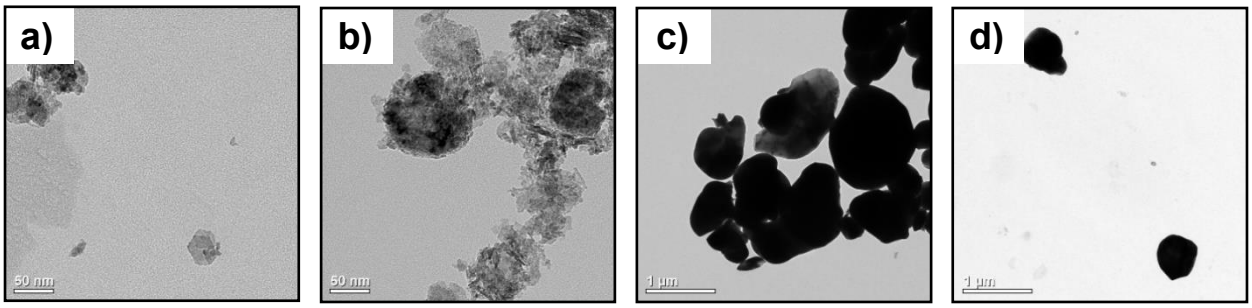

Figure S2. Transmission electron micrographs of a) 333 NMC, b) 622 NMC, c) c622 NMC, and d) c811 NMC.

S6. Scanning Electron Microscopy of Nanoscale NMC

To characterize the morphology of the 333 and 622 NMC nanosheets, a methanolic colloidal suspension of each NMC was made and drop-cast onto boron-doped Si wafers. For imaging, a Leo Supra55 VP scanning electron microscope (SEM) was used with a standard in-lens detector (3 kV incident electron energy).

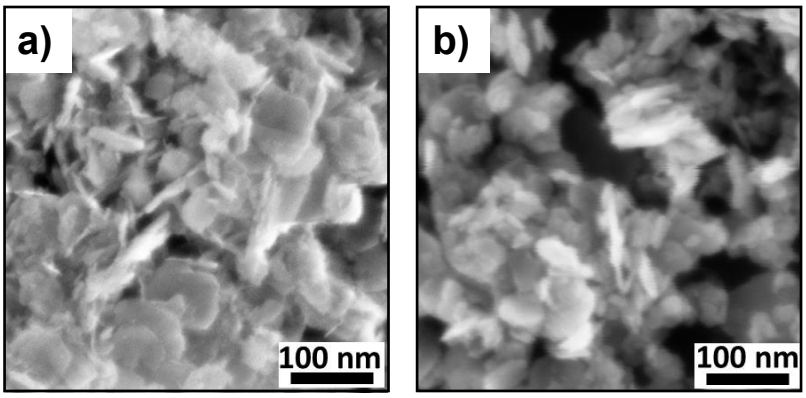

Figure S3. Scanning electron micrographs of a) 333 NMC and b) 622 NMC.

S7. Zeta Potential of NMC in Each Media

Table S1. Zeta potential measured for the different NMC compositions in bacterial medium and daphnid medium.

	Zeta Potential (mV)			
NMC Type	**333**	**622**	**c622**	**c811**
Bacterial medium	-13±3	-12±1	-21±3	-23±1
Daphnid medium	0±5	-1±3	-14±6	-15±2

S8. Models of Li-terminated and H-terminated Surfaces of Ni-enriched NMC

The NMC surface slabs used in this work, as in those modeled previously,[2,3] have four O-*TM*-O layers. In this surface slab, the two interior (bulk-like) and two exterior layers (surface) are related by inversion symmetry. The surface cells are based on a $\left[\sqrt{3} \times \sqrt{3}\right]$R30° rotated modification of the lithium cobalt oxide primitive unit cell. In order to model step-wise cation release, both Li- and H-terminated surfaces are modeled (Figure S4), as detailed in previous work.[2,3] In all NMC structures investigated here, surface lithium are above a 3-fold hollow site and hydrogen are above an oxygen, forming an OH bond. Each supercell surface slab has in-plane lattice dimensions of either $2\sqrt{3}\mathrm{a} \times \sqrt{3}a$ or $3\sqrt{3}\mathrm{a} \times \sqrt{3}a$, where a=2.883 Å and cells have at least 15 Å of vacuum between surface slabs. Surface relaxations employ either a 3×6×1 *k* or 2×6×1 *k*-point grid[4] for the $2\sqrt{3}\mathrm{a} \times \sqrt{3}a$ or $3\sqrt{3}\mathrm{a} \times \sqrt{3}a$ slabs, respectively.

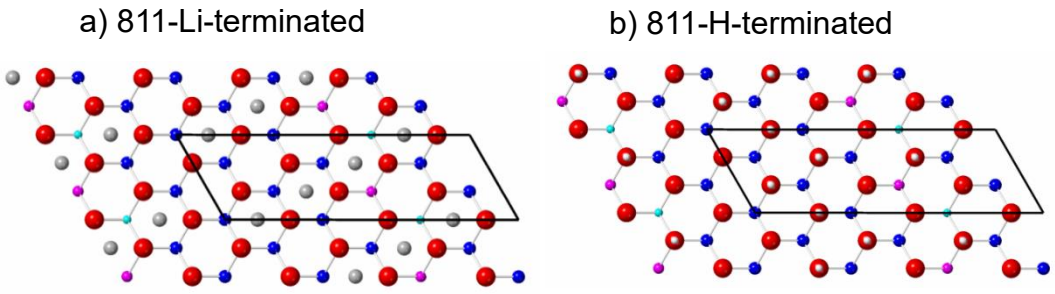

Figure S4. Computational models of Ni-enriched NMC surfaces with different terminations. Top-down views of representative a) Li-terminated and b) H-terminated Ni-enriched NMC surfaces. Lithium (gray) is found above a 3-fold hollow surface site and hydrogen (white) is located directly above an oxygen in the surface layer, forming an OH bond. Oxygen is red and the transition metals in the subsurface layer are depicted as follows: nickel is dark blue, manganese is magenta, and cobalt is cyan.

S9. Determination of ΔG Values Used for Computational Modeling

Zero-point energy (ZPE) correction terms are added to the DFT total energies of Ni-enriched NMC slabs to obtain $\Delta G_1 = E_{products} - E_{reactants} + ZPE$, as described in the literature.[19,28] The total energies of lithium, transition metals (*TM*), oxygen, and hydrogen released from the surface are for the atoms in their standard state, which implies that ΔG_1 can be used to gauge relative lattice stabilities for the overall release of a *TM*-OH unit.

The second term in the model, ΔG_2, is based on the Nernst equation, $\Delta G_2 = \Delta G^0_{SHE} - n_e e U_{SHE} - 2.303 n_{H^+} kT\, pH + kT \ln a\left(H_x AO_y^{z-}\right)$, where ΔG^0_{SHE} is the change in free energy of the aqueous cation/anion relative to the standard state, and these values are referenced to the standard hydrogen electrode (SHE). The values of ΔG^0_{SHE} used in this work are obtained from literature[5] and are found in Table S2. eU_{SHE} is the applied potential, relative to the SHE, and it is assumed that no external potential is applied ($eU_{SHE} = 0$). $H_x AO_y^{z-}$ are the concentrations of the released aqueous ions, and that these concentrations are 1×10^{-6} M; this is the order of magnitude in line with measurements of released cations reported in experiment.[31,32] The n_e and n_{H^+} terms denote the number of electrons and protons involved in the chemical reactions required for surface release. The pH-independent species are Li^+, Ni^{2+}, Mn^{2+}, and Co^{2+}, and the pH dependent species are $HCoO_2^-$, and oxygen and hydrogen, as H_2O, in the range of pH 1-9 investigated here.

At conditions of $eU_{SHE} = 0$ and $a = 1 \times 10^{-6}\ M$, DFT-calculable Pourbaix diagrams[6] show that $Ni^{2+}_{(aq)}$ will be the preferred aqueous cation of nickel until ~pH 9.5 when $NiO_{(s)}$ will precipitate, $Mn^{2+}_{(aq)}$ will be dominant until ~pH 10, when $Mn_2O_{3(s)}$ or $Mn_3O_{4(s)}$ will precipitate, and $Co^{2+}_{(aq)}$ will be dominant until pH 7, where $Co^{2+}_{(aq)}$ reacts further with H_2O to produce $HCoO_2^-{}_{(aq)}$. $HCoO_2^-{}_{(aq)}$ becomes the preferred aqueous ion of cobalt at pH 7, and the dramatic change in thermodynamics of cobalt speciation, $Co^{2+}_{(aq)}$ $\left(\Delta G^0_{SHE} = -0.563\right)$ vs. $HCoO_2^-{}_{(aq)}$ $\left(\Delta G^0_{SHE} = -4.223\right)$, will be present as a discontinuity at pH 7.

Table S2. ΔG_2 for each aqueous species used in the surface metal release of Ni-enriched NMC. The values of ΔG^0_{SHE} are taken from previous work[5] and converted to eV. For all calculations presented in the manuscript, U_{SHE} is 0 and the concentration of each species, $a_{H_xAO_y^{z-}}$, is assumed to be 1×10^{-6} M.

Element	Aqueous Species	$\Delta G^0_{SHE}\ (eV)$	$\Delta G_2\ (eV)$
Li	Li^+	-3.039	$-1eU_{SHE} + 0.0257lna_{Li^+} - 3.039$
Ni	Ni^{2+}	-0.472	$-2eU_{SHE} + 0.0257lna_{Ni^{2+}} - 0.472$
Mn	Mn^{2+}	-2.363	$-2eU_{SHE} + 0.0257lna_{Mn^{2+}} - 2.363$
Co	Co^{2+}	-0.563	$-2eU_{SHE} + 0.0257lna_{Co^{2+}} - 0.563$
Co	$HCoO_2^-$	-4.223	$-2eU_{SHE} - 0.177pH + 0.0257lna_{HCoO_2^-} - 4.223$
O	H_2O	0	$2eU_{SHE} + 0.118pH$
H	H_2O	0	$-0.059pH$

S10. Impact of Bacterial Presence on Dissolution of Commercial NMC

To investigate the assumption that the presence of bacteria has no impact on NMC dissolution, dissolution studies were run as described in the main text, with some trials being done in the presence of bacteria. The bacteria were diluted to an OD of 0.1 (~10^8 cells/mL) in bacterial medium, and then 1.35 mL of bacterial suspension or bacterial medium were mixed with 0.15 mL of c622 or c811 NMC so that they were at 2.8 m^2/L doses. The exposure lasted for 3 hours, and then the samples were centrifuged at 4696×*g* for 30 min, followed by a 10-fold dilution of the supernatant with bacterial medium prior to centrifuging again at 286,000×*g* for one hour. The supernatants were then analyzed with a Thermo Scientific Xseries-2 ICP-MS.

The dissolution of commercial NMC materials appeared to be minimally influenced by the presence of bacteria (Figure S5). The dissolved concentrations of the metals appear to be

unchanged with the exception of lithium and nickel from c811 NMC. The difference in lithium release is a 3% reduction in the presence of the bacteria, whereas approximately 10% reduced nickel is released from c811 NMC in the presence of bacteria. While statistically significant, when used in a toxicity experiment, these differences are not likely to impact the outcome of *S. oneidensis* exposure, as can be seen in the ion toxicity data in the main text.

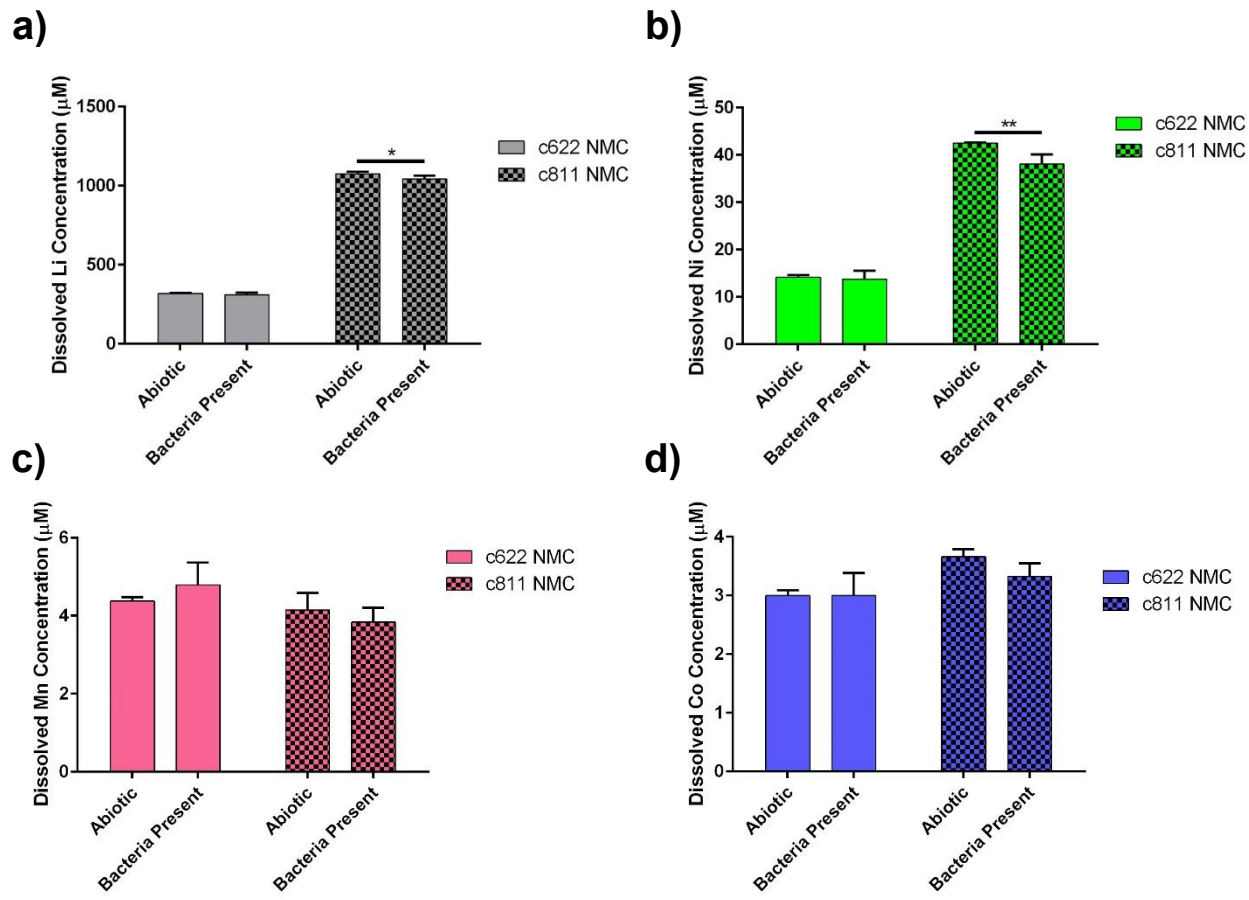

Figure S5. The influence of bacteria presence on the dissolution a) lithium, b) nickel, c) manganese, and d) cobalt from c622 and c811 NMC. The error bars represent the standard deviations of three replicates. Statistical testing was done using a two-way ANOVA with Sidak's multiple comparisons test.

S11. Toxicity of commercial NMC to *S. oneidensis* MR-1

The toxicity of the commercial materials was assessed using the same growth based viability assay that was described in the main text.[7] Briefly, the bacteria were exposed to commercial materials at surface area-based doses ranging from 0-2.8 m^2/L for 3 hours. After the exposure, they were transferred to LB broth and allowed to grow overnight, monitoring the optical density of

the suspension every 20 min. The growth curves were then analyzed with the R package provided in the literature[7] to determine the viability of the bacteria at the end of the exposure period.

It can be seen that the commercial NMC materials demonstrated similar toxicity to *S. oneidensis* as the nanoscale NMC materials (Figure S6). These results are surprising, because nickel and cobalt are the toxic components of these materials to *S. oneidensis*; it would be expected that as nickel content was increased, there would be a corresponding increase in the toxicity of the material as well. To understand this observation, the dissolution behavior of the materials were investigated using a computational chemistry approach as well as an experimental approach, the results of which can be found in the main text.

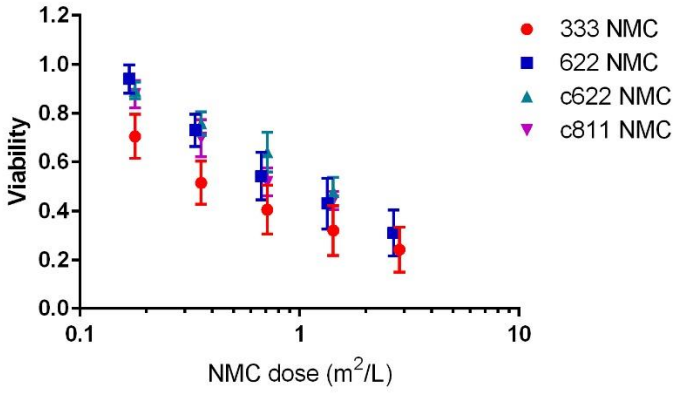

Figure S6. The toxicity of the commercially available NMC materials also matches that of the lab-synthesized 333 and 622 NMC when the dosage is normalized by surface area. Please note that the data for 333 and 622 NMC is recapitulated from the main text to facilitate comparison. The error bars represent the standard error of seven (333, 622 NMC) or three (c622, c811 NMC) replicates.

S12. Comparison of ΔG_3 Values Determined by PBE and B3LYP

DFT results for ΔG_3 are benchmarked for different exchange-correlation functionals. We have utilized a pure GGA functional; PBE, and a hybrid functional; B3LYP. Our results indicate that the overall trends of the calculated ΔG_3 values are not sensitive towards the choice of the exchange-correlation functional. For all the transition metals and functional types, a bi-lactate ligated structure is more energetically favorable than a mono-lactate ligated complex. Except for [Co(LA)(H_2O)$_4$), PBE systematically underestimates the ΔG_3 compared to B3LYP. Nevertheless, relative stabilities are the same for both functional types.

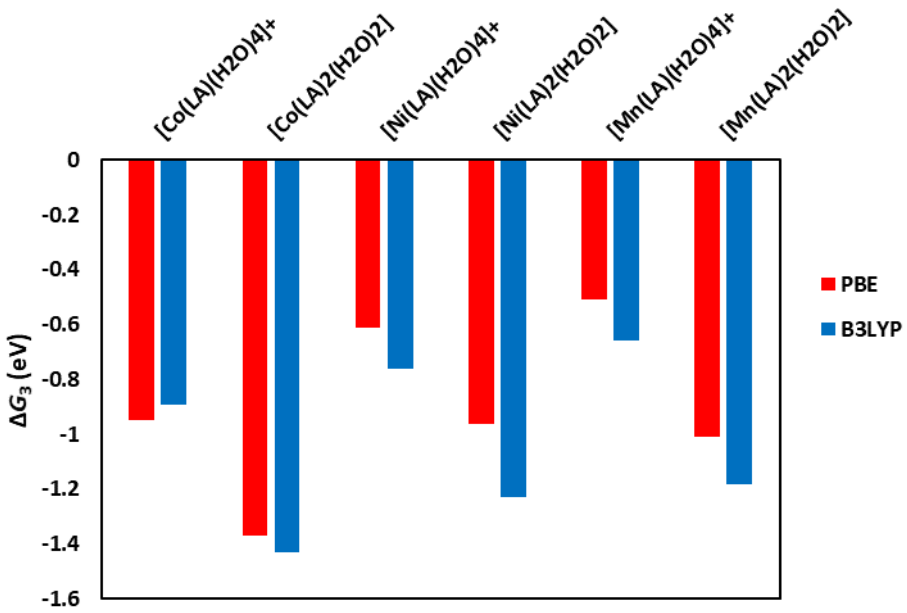

Figure S7. Comparison between PBE and B3LYP calculated values of ΔG_3.

S13. Association of commercial NMC to *S. oneidensis* MR-1

The association of the commercial materials was investigated as described in the main text for the nanoscale NMC, using both TEM and hyperspectral imaging techniques (Figure S8). For the microscale materials (c622 and c811 NMC), very little if any binding is observed in the TEM images acquired; this does not preclude the fact that there may be binding, it merely suggests that it is very rare. However, when looking at the hyperspectral images, where the signals are falsely colored to depict bacteria (red) and NMC material (green), it can be seen that there is more extensive colocalization of these materials with bacteria than has been previously observed. In fact, where large pieces of NMC can be seen in the images, it appears as though the bacteria are swarming around it and possibly attaching to it, as indicated by the fact that there are extensive red regions around the large green regions.

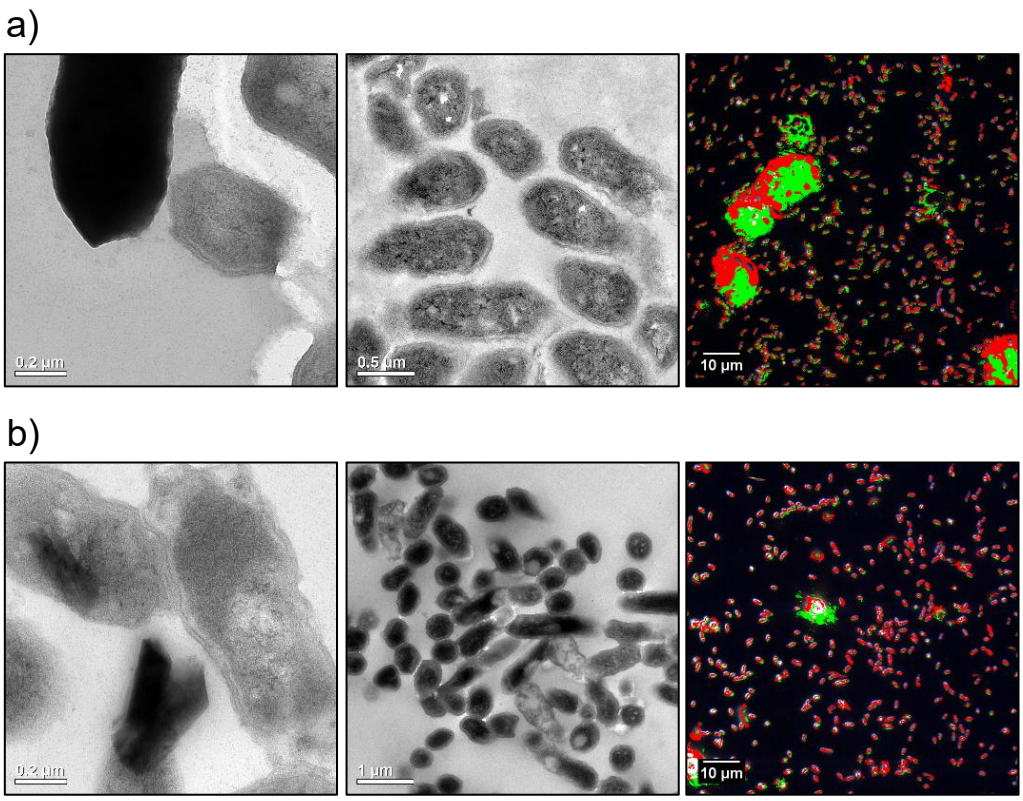

Figure S8. The association of bacteria to a) c622 NMC and b) c811 NMC were investigated using TEM and hyperspectral imaging. (Left column) Zoomed in TEM images depicting commercial NMC materials in close proximity to bacteria and (middle column) zoomed out TEM images showing that such interactions are rare to see. (Right column) Hyperspectral images that show the colocalization of commercial NMC materials with bacteria; pixels that are falsely colored as red indicate bacteria and pixels that are falsely colored as green indicate NMC.

S14. Toxicity of commercial NMC to *D. magna*

Daphnid neonates were exposed to commercial NMC materials for 48 hours by placing them in 10 mL solutions that contained 5 mL of 2× daphnid medium, the appropriate volume of 50 mg/L NMC solution, and Milli-Q water. The daphnids were exposed to commercial NMC at concentrations ranging from 0-0.024 m^2/L (corresponding to mass-based doses ranging from 0-10 mg/L). Practical limitations precluded the use of commercial, microscale materials at matching surface area doses to daphnids because the low surface area would require large masses of commercial NMC to be suspended in solution, which is why these materials were used at matching mass-based doses to the nanoscale materials in the main text. Four replicate experiments were done, with 5 daphnids per replicate, following OECD guideline 202. No food

was added to the experiment during the exposure time, and daphnid survival was recorded at 24 and 48 hours. At equivalent mass-based doses, there was no toxicity observed from any of the commercially available, microscale materials (Figure S9). This is likely due to the small doses that could be used for these experiments.

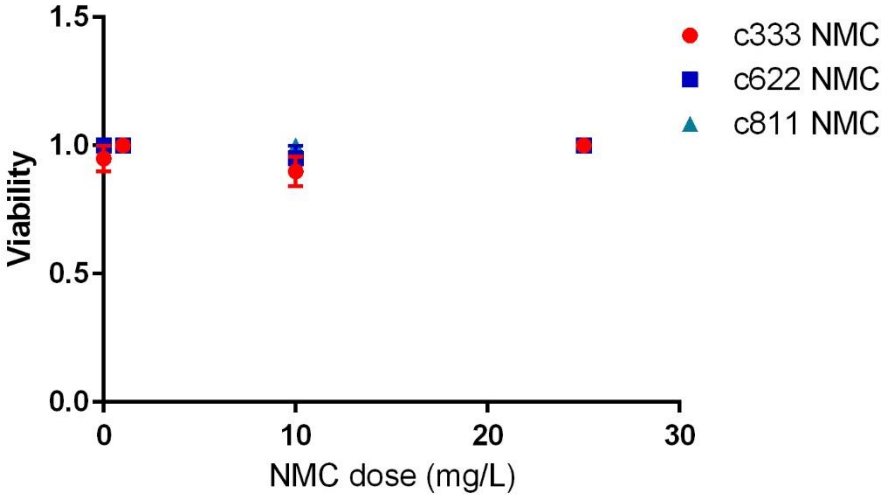

Figure S9. Assessment of daphnid survival after 48 hours of exposure to commercial 333 NMC, commercial 622 NMC, and commercial 811 NMC. None of the commercial NMC materials were found to be toxic to the daphnids with a two-way ANOVA. The error bars in these graphs represent the standard error from four exposure replicates. The error bars are not visible for some data points due to all of the daphnids surviving the exposure.

S15. Association of commercial NMC to daphnids

The association of the commercial NMC was investigated using brightfield microscopy. From these images, it can be seen that most of the commercial NMC have been ingested and are visible in the darkened gut of the daphnids. This is different from what was seen with the nanoscale NMC materials, in which the NMC was mostly adhering to the daphnid carapace. The discrepancies in the behavior of these materials is likely due to an interplay between the surface charge and size of the nanomaterials. It has previously been shown that positively charged NPs are more toxic than negatively charged NPs to daphnids,[8] in part due to the higher affinity of positively charged particles for the negatively charged surface of the cell membrane. The nanoscale materials used here exhibited a neutral ζ-potential in daphnid medium whereas the microscale materials had a

negative surface charge, which could explain the observed association patterns. The size differences also likely play a role here, since it was observed that the larger particles settled to the bottom of the beaker more quickly than the nanoscale materials. Daphnids are also capable of more efficiently ingesting larger particles,[9] consistent with what is observed here. It is worth noting that association of 622 NMC to *D. magna* was consistently more prevalent than 333 NMC, and there are also some of both NMC nanomaterials visible in the daphnid gut.

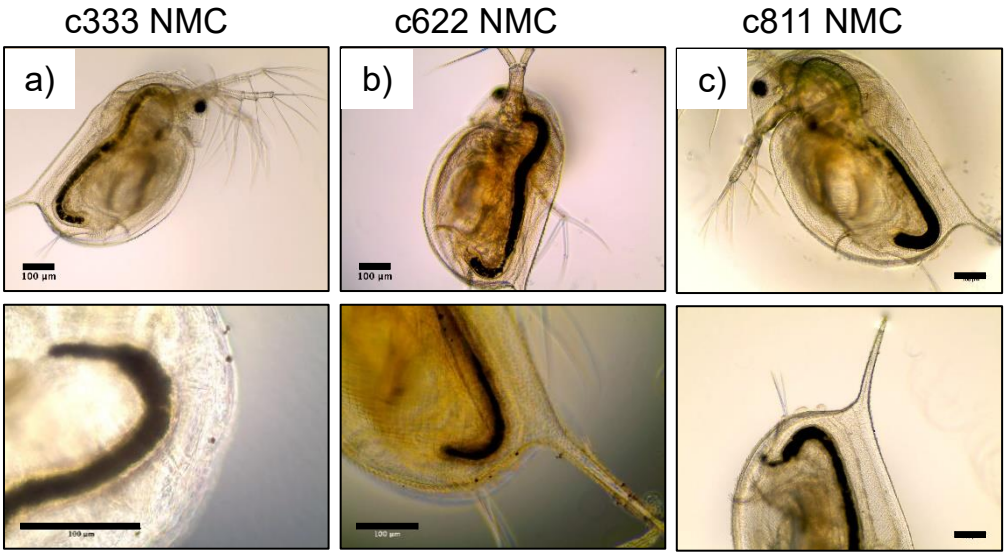

Figure S10. Brightfield images depict daphnid interaction with a) commercial 333 NMC, b) commercial 622 NMC, and c) commercial 811 NMC, which demonstrates that the majority of the NMC ends up in the daphnid gut. Zoomed in images (bottom row) highlight the darkened gut of the animal, indicating that the NMC had been ingested. The scale bars here all indicate 100 µm.

References

1 P. Hovington, V. Timoshevskii, S. Burgess, H. Demers, P. Statham, R. Gauvin and K. Zaghib, Can we detect Li K X-ray in lithium compounds using energy dispersive spectroscopy?, *Scanning*, 2016, **38**, 571–578.

2 J. W. Bennett, D. T. Jones, R. J. Hamers and S. E. Mason, First-principles and thermodynamics study of compositionally tuned complex metal oxides: cation release from the (001) surface of Mn-rich lithium nickel manganese cobalt oxide, *Inorg. Chem.*, 2018, **57**, 13300–13311.

3 J. W. Bennett, D. Jones, X. Huang, R. J. Hamers and S. E. Mason, Dissolution of complex

metal oxides from first-principles and thermodynamics: cation removal from the (001) surface of $Li(Ni_{1/3}Mn_{1/3}Co_{1/3})O_2$, *Environ. Sci. Technol.*, 2018, **52**, 5792–5802.

4 H. J. Monkhorst and J. D. Pack, Special points for Brillouin-zone integrations, *Phys. Rev. B*, 1976, **13**, 5188–5192.

5 D. D. E. Wagman, I. Halow, V. B. Parker, S. M. Bailey and R. H. Schumm, Selected Values of Chemical Thermodynamic Properties, *Natl. Bur. Stand.*

6 K. A. Persson, B. Waldwick, P. Lazic and G. Ceder, Prediction of solid-aqueous equilibria: scheme to combine first-principles calculations of solids with experimental aqueous states, *Phys. Rev. B*, 2012, **85**, 235438.

7 T. A. Qiu, T. H. T. Nguyen, N. V. Hudson-Smith, P. L. Clement, D.-C. Forester, H. Frew, M. N. Hang, C. J. Murphy, R. J. Hamers, Z. V. Feng and C. L. Haynes, Growth-based bacterial viability assay for interference-free and high-throughput toxicity screening of nanomaterials, *Anal. Chem.*, 2017, **89**, 2057–2064.

8 J. S. Bozich, S. E. Lohse, M. D. Torelli, C. J. Murphy, R. J. Hamers and R. D. Klaper, Surface chemistry, charge and ligand type impact the toxicity of gold nanoparticles to *Daphnia magna*, *Environ. Sci. Nano*, 2014, **1**, 260–270.

9 S. Rist, A. Baun and N. B. Hartmann, Ingestion of micro- and nanoplastics in *Daphnia magna* – quantification of body burdens and assessment of feeding rates and reproduction, *Environ. Pollut.*, 2017, **228**, 398–407.